Corrosion Science 172 (2020) 108743

Contents lists available at ScienceDirect

Corrosion Science

journal homepage: www.elsevier.com/locate/corsci

Access to nanocrystalline, uniform, and fine-grained Ni-P coating with improved anticorrosive action through the growth of ZnO nanostructures before the plating process

Zahra Sharifalhoseini[a,*], Mohammad H. Entezari[a,*], Ali Davoodi[b,c], Mohsen Shahidi[d]

[a] Sonochemical Research Center, Department of Chemistry, Ferdowsi University of Mashhad, 91775, Mashhad, Iran
[b] Metallurgical and Materials Engineering Department, Faculty of Engineering, Ferdowsi University of Mashhad, Mashhad, 91775-1111, Iran
[c] John A. Paulson School of Engineering and Applied Sciences, Harvard University, 29 Oxford Street, Cambridge, Massachusetts 02138, United States
[d] Samed Chemical Industries Company, Mashhad, Iran

ARTICLE INFO

Keywords:
ZnO nanoflakes
Surface modification
Fine-grained Ni-P deposit
Corrosion resistance

ABSTRACT

In this work, the mild steel surface was modified by the growth of ZnO nanoflakes through a feasible and scalable procedure. The modified surface was used for the coating by the electroless nickel (EN) plating, and the influence of this modification on the morphology, surface roughness, uniformity, the corrosion behavior of Ni-P coating, and also on the deposition rate of EN plating was studied. The SEM micrographs, especially backscatter images, disclosed that the matrix of Ni-P coating with the underneath of ZnO NSs possesses smaller grain size with more uniform distribution compared to the specimen without ZnO NSs. The AFM analysis affirmed the lower surface roughness of this sample. The results of the EIS measurements and the Tafel extrapolation method indicated that the corrosion resistance of this sample is approximately two times higher than that of the sample without zinc oxide (Rp ≈ 35,000 Ω cm^2). The role of ZnO NSs in increasing the active nucleation density and the formation of uniform, compact, and fine-grained Ni-P deposit was discussed. Besides, the effects of ZnO NSs on generating scattering centers, restricting the electron transfer, strengthening the Ni-P matrix, and the consequent corrosion behavior, were investigated.

1. Introduction

Nanotechnology encompasses a wide range of disciplines, including surface science, chemistry, biology, physics, and engineering. This advanced technology by manipulating materials in nanoscale presents a broad spectrum of nanomaterials with unique properties [1]. In this field of science, various techniques have been developed for the production of inorganic nano-structured materials such as titanium dioxide, zinc oxide, silver, copper, gold particles, and carbon nanotubes [2,3]. Among inorganic materials, ZnO has drawn considerable attention from scientists, due to its safety, nontoxicity, good biocompatibility, and chemical stability [4–7]. Concerning these properties, a large amount of research has been conducted on the preparation of the modified paper, glass, textile, and metal surfaces with zinc oxide nanostructures (ZnO NSs) for medical purposes [8–15]. The usage of ZnO for tissue engineering can be cited as another example in this field [16–18].

In parallel to these scientific reports, other studies have highlighted the electron communication feature of zinc oxide. For instance, Zhuang et al. manipulated the photoresponsivity of FTO surface by the synthesis of ZnO NSs for the access of photoanodes in dye-sensitized solar cells [19], and Zhu et al. prepared sensitized-type solar cells based on ZnO photoanode using the ultrasonic spray pyrolysis technique [20]. In addition, this metal oxide as a very important II–VI semiconductor has been used for the photocatalytic degradation of organic and inorganic pollutants (e.g. arsenitite, phthalic acid, Rhodamine B, and phenolic compounds) [21–24]. Controlling the wettability and superhydrophobicity of different substrates by the ZnO deposition has been reported in the literature [25–28].

Zinc oxide as an anticorrosive pigment has been developed in the matrix of organic coatings [29,30], but this ceramic oxide has been less used to improve the corrosion resistance of metals and alloys [31,32].

In this research, we have focused on anticorrosive action of ZnO to modify the mild steel surface and improve the corrosion resistance. Over the years, researchers around the world have devoted considerable efforts to reduce the astoundingly high cost of corrosion. In this

* Corresponding authors.
E-mail addresses: z.sharif@um.ac.ir (Z. Sharifalhoseini), entezari@um.ac.ir (M.H. Entezari).

https://doi.org/10.1016/j.corsci.2020.108743
Received 4 December 2019; Received in revised form 26 April 2020; Accepted 13 May 2020
Available online 16 May 2020
0010-938X/

regards, finding or improving protective coatings is a one of the most important preventive strategies [33,34]. Binary Ni–P deposits, which are produced by electroless technique, have been extensively developed for a wide range of engineering applications. Up to now, a substantial amount of research has been carried out on the improvement in the structure and anticorrosive action of electroless Ni-P deposits [35–37].

In the past decades, successful strategies have been employed to produce ZnO micro/nanostructures with different morphologies on various surfaces. Along with solution-based approaches such as hydrothermal, solvothermal, sol-gel and electrochemical methods [38–41], some other procedures, including molecular beam epitaxy (MBE) [42], pulsed laser deposition (PLD) [43], chemical vapor deposition (CVD) [44], and magnetron sputtering have been applied to grow or deposit ZnO thin films [45]. It has been reported that the electrochemical method eliminates the need for sophisticated instruments and the complexity of some procedures used to grow or deposit nanomaterials [46,47]. The cyclic voltammetry (CV) as a powerful electrochemical technique has been employed to deposit ZnO films [48,49]. In the present work, this method has been applied for the growth of ZnO nanostructures on the mild steel surface. As a practical application, the surface containing zinc oxide has been used as a modified surface for the electroless Ni-P (EN) plating, and the influence of this modification over the morphology, surface roughness, grain size and the anticorrosive action of Ni-P coating has been studied.

2. Experimental

2.1. Materials

Chemicals, including hydrochloric acid (HCl, 12 mol L^{-1}), phosphoric acid (H_3PO_4, 85 %) for surface activation, zinc sulfate heptahydrate ($ZnSO_4$. $7H_2O$) for ZnO synthesis, and sodium chloride (NaCl) for the corrosion test were purchased from Merck and used without purification. The chemical composition of the metal substrate (in wt. %), which is determined by a Quantometer (3460ARLFISONS), as follows: Fe - 99.340, Mn - 0.387, Al - 0.059, Si - 0.058, Cu - 0.043, Cr - 0.028, C - 0.024, S - 0.033, Ni - 0.031, P - 0.013, Co - 0.007, Sn - 0.001, Mo - 0.001 Ti - 0.001.

2.2. Pretreatment of the steel surface

The surface pretreatment is a critical step because the presence of non-active regions on the surface results in failure in the coating process. For the surface activation, the sample with the dimensions 20 mm × 20 mm × 1 mm, after cleaning with acetone and rinsing with distilled water, was placed in a beaker containing concentrated acid (HCl, 12 mol L^{-1}) for 30 s. To produce a more uniform roughness, the plate was then immersed into a beaker containing 100 ml of diluted hydrochloric acid (0.1 mol L^{-1}) and irradiated by an ultrasonic bath (40 kHz, Branson 8510E-DTE, internal dimensions: 49 cm × 29 cm × 16 cm) at 40 °C. After 10 min, the plate was removed and washed with distilled water. Note that the activated surface should be used immediately because the surface is very susceptible to oxidation.

2.3. ZnO synthesis

For the synthesis of ZnO NSs, the cyclic voltammetry (CV) technique was applied. A conventional three-electrode set up (SAMA 500, electroanalyzer system), including Ag(s)|AgCl(s)|Cl^- (aq., saturated KCl) as the reference electrode, a thin sheet of platinum (with the dimensions 9 mm × 19 mm) as the auxiliary electrode and the mild steel as the working electrode, was used for the electro-synthesis. CV experiments were carried out by scanning the potential from -1.2 to -1.0 V for 25 cycles with a scan rate of 0.1 V s^{-1}. Additionally, an electrochemical cell with a trapezoidal shape was used as the reaction vessel, and the temperature was adjusted at 50 °C by a water bath. The surface of 1.5 cm^2 of the mild steel was exposed to the electrolyte (100 ml of $ZnSO_4$ solution, 5 mmol L^{-1}). After the ZnO growth, the sample was dried in an oven at 100 °C for 1 h. The operating conditions of the electro-synthesis are given in Table 1.

Table 1
Operating conditions of the ZnO electro-synthesis.

Parameters	Amount
Electrolyte, conc.	$ZnSO_4$, 5 mmol L^{-1}
Temperature	50 ± 2 (°C)
Potential range	−1.2 to −1.0 (V)
Scan rate	0.1 V/s
Cycle number	25
Working electrode	mild steel
Reference electrode	Ag(s)|AgCl(s)|Cl^- (aq., saturated KCl)
Auxiliary electrode	Thin sheet of platinum

2.4. The electroless Ni-P coating

Because of the dissolution of zinc oxide at pH < 6, the acid baths are not suitable for EN plating [50]. Therefore, a basic bath was prepared to have stable ZnO NSs. The composition and operating conditions applied for the EN plating are summarized in Table 2.

In the applied bath, nickel sulfate was used as the source of Ni^{2+} ions, sodium citrate as the complexing agent and sodium hypophosphite as the reducing agent. In addition, a small amount of lead acetate was added to the bath as the stabilizer, and the pH was adjusted at 8.0–8.3 with ammonia. The coating was also performed for another activated sample without ZnO NSs to find the influence of ZnO NSs over the properties of Ni-P coating. The steel after EN plating was named as "*SEN*", and steel containing ZnO after the coating was labeled as "*SZEN*".

2.5. Corrosion study

Potentiodynamic polarization (PDP) tests were performed by the same three-electrode set up used for the ZnO electro-synthesis (described in Section 2.3). After immersing the working electrode into the corrosive medium (NaCl, 3.5 %), the sample was left to stabilize for 10 min. For PDP tests, the potential was applied in the range of -250 to +250 mV around the open circuit potential (E_{OCP}) with the scan rate of 1.00 mV/s. All measurements were made at room temperature (≈ 20 °C), and area of 1 cm^2 of the specimen was exposed to the electrolyte and other parts of the surface were isolated by the epoxy resin.

For the EIS analysis, a potentiostat/galvanostat (Autolab 302 N) was used, and measurements have been taken in the frequency range of 100 kHz to 0.1 Hz with an amplitude of 10 mV at the open circuit potential. All measurements were performed at the room temperature (≈ 20 °C).

3. Results and discussion

3.1. Characterization of the coatings

The morphology of samples, including sono-treated sample, ZnO deposited alloy, and EN plated samples (*SEN* and *SZEN*), was monitored

Table 2
Composition and deposition parameters of the used bath.

Deposition parameters	Amount
Nickel sulfate	2.5 (g/100 ml)
Sodium citrate	1.5 (g/100 ml)
Sodium hypophosphite	2.75 (g/100 ml)
Temperature	85 ± 2 (°C)
Time	15 min
pH	8.0–8.3

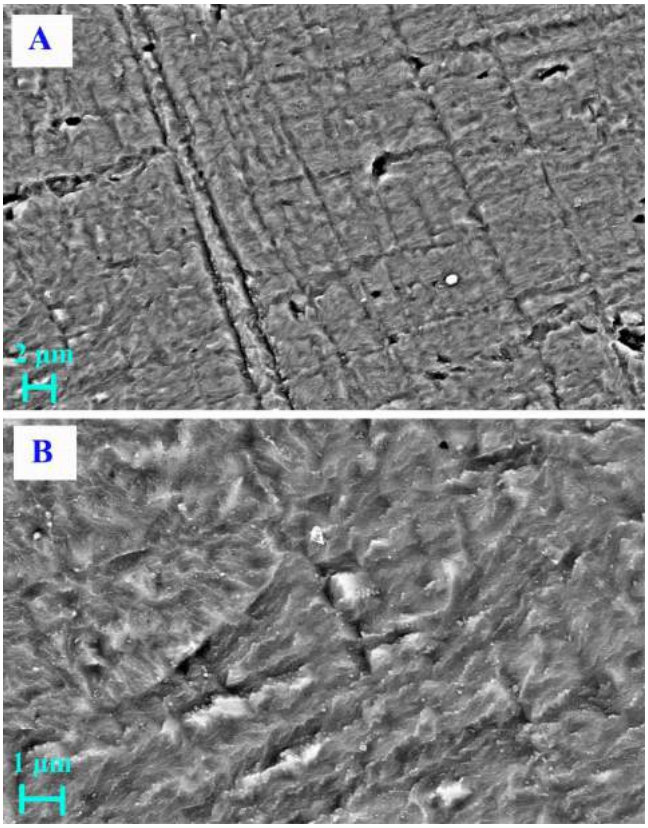

Fig. 1. The surface morphology of sonochemically pretreated surface at different magnifications.

by a field emission scanning electron microscope (FE-SEM, Tescan Mira 3 LMU), and the elemental composition was determined by the EDS system (attached to the SEM).

3.1.1. SEM analysis

The SEM images of mild steel surface before any pretreatment were shown in the supplementary data (Fig. S1). This figure exhibits that the surface is not smooth. Depressions on the surface are attributed to the alloy manufacturing process. The sono-chemically pretreated surface is depicted in Fig. 1.

Fig. 1(A) and (B) reveals that the ultrasonic irradiation creates the proper roughness on the overall surface. Micro and especially nano-sized roughness formed during the pretreatment process is of critical importance to the coating process because it leads to the increased contact surface area between the base substrate and the upper layer. Additionally, the equal distribution of activated regions on the surface has a positive effect on active nucleation site density and the consequent uniform growth of zinc oxide structures.

SEM images of the as-grown ZnO film are exhibited in Fig. 2.

As seen in Fig. 2(A–C), the flake-like structures of ZnO are synthesized on the activated surface (elemental analysis confirmed the presence of zinc and oxygen, see Section 3.1.2). From micrographs, the thickness of flakes is estimated about 50 − 80 nm (Fig. 2(C)). In addition, some small ZnO nanoflakes (marked with green arrows) can be observed in this figure.

The surface morphology of the *SEN* and *SZEN* are displayed in Figs. 3 and 4, respectively. In both figures, (A') and (B') are back backscatter images of (A) and (B), and (C') is a magnified view of the red shape marked on the image (B).

The back backscatter images are provided to have a better sight of grain boundaries. In comparison with *SEN*, *SZEN* is more uniform. The electroless Ni deposit of *SEN* is coarse, and many grains larger than one

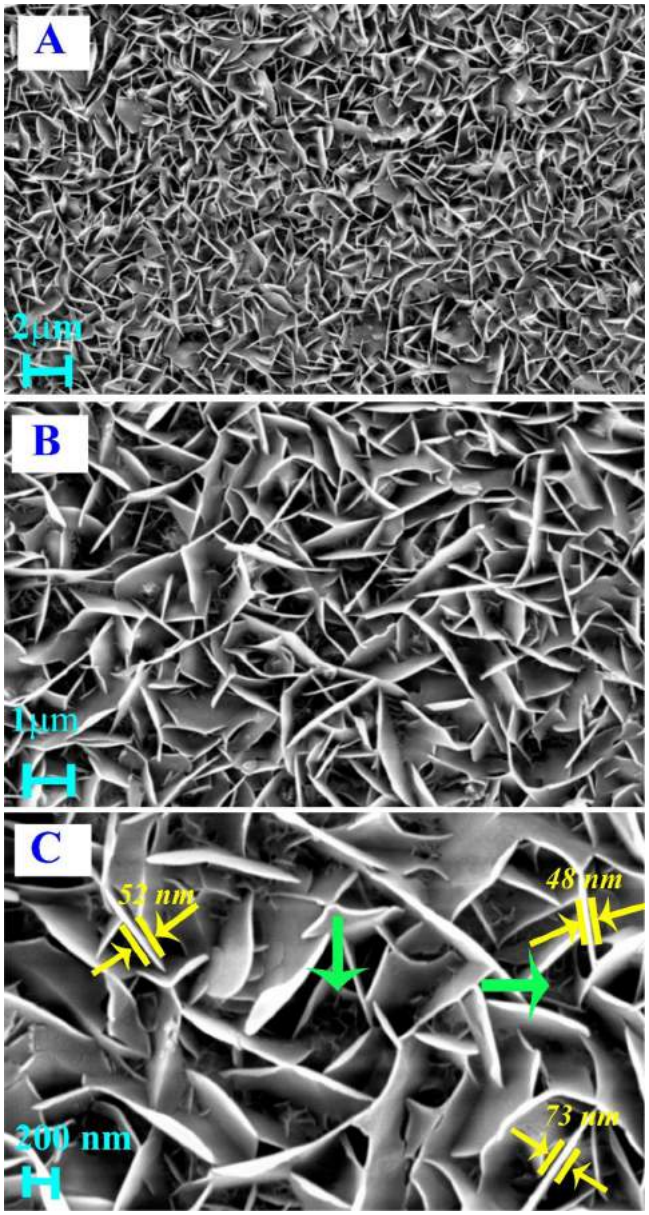

Fig. 2. SEM images of the as-grown ZnO film: (A), (B), and (C) are attributed to the magnifications of 10,000 ×, 25,000 ×, and 50,000 ×, respectively.

micron are observed whereas *SZEN* is mostly covered with a fine-grained Ni layer (the size of most grains are less than 1000 nm).

3.1.2. EDS analysis

The EDS spectrum and the elemental analysis of the ZnO deposited surface are given in the supplementary data (Fig. S2). The detection of zinc and oxygen in the sample is considered as the evidence for the formation of zinc oxide phase.

The EDS microanalysis of samples *SEN* and *SZEN* are also provided in the supplementary data (Figs. S3 and S4, respectively). The EDS element maps disclose the distribution of nickel and phosphorus is homogenous, and the elemental analysis shows a range of 8–9 percent weight of phosphorus in EN films. Therefore, the resulting coatings can be classified into the medium phosphorus electroless nickel category. This classification has a smaller crystalline size and tends to be semi-amorphous compared to low-phosphorous deposits (1–4% P) [51].

3.1.3. XRD analysis

The crystal structure of ZnO deposited sample recorded by an X-ray

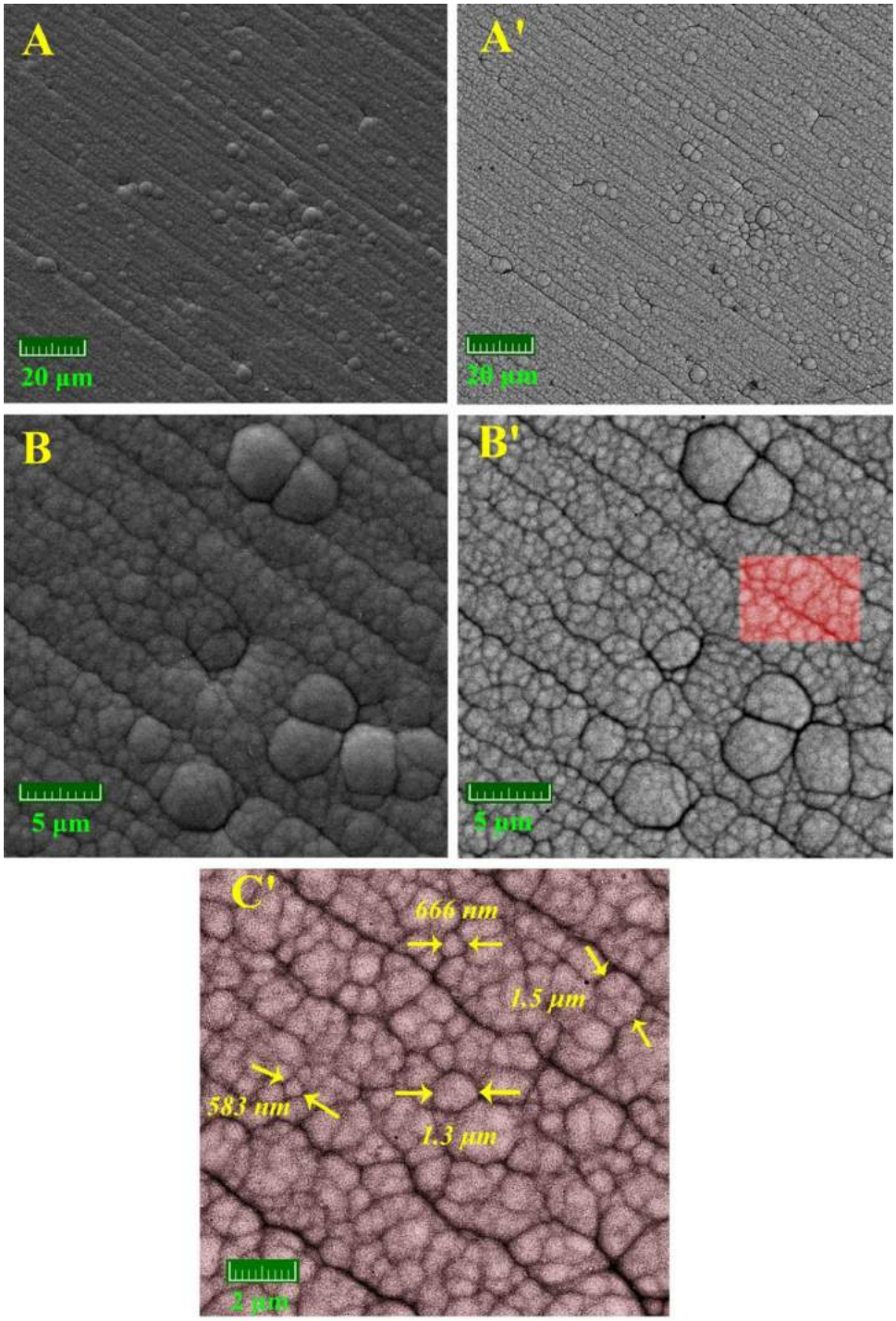

Fig. 3. The morphology of *SEN*: (A') and (B') are back backscatter images of (A) and (B), and (C') is a magnified view of the red shape marked on the image (B). (For interpretation of the references to colour in this figure legend, the reader is referred to the web version of this article).

diffraction spectrometer (XRD Explorer, GNR, Italy) with CuKα radiation (λ = 0.154 nm) confirms the formation of the pure phase of zinc oxide (Fig. 5).

This pattern exhibits diffraction peaks of ZnO, corresponding to the planes (1 0 0), (0 0 2), (1 0 1), (1 0 2), (1 1 0), (1 0 3), (2 0 0), (1 1 2), (2 0 1), and (2 0 2). The pattern is matched with the ICCD no: 96-210-7060. Note that green stars indicate diffraction peaks of iron (as the substrate) at 2θ = 44.79 and 65.31°. The XRD pattern is matched with the ICCD no: 96-411-3933.

3.1.4. AFM analysis

The roughness of the sono-treated sample and the ZnO deposited surface was studied, and the results are shown in Fig. 6.

In this figure, (A) and (B) are attributed to face projections of sono-treated sample and the ZnO deposited surface, respectively. Besides, 3D topographies and 3D phase images of each specimen are labeled by the (′) and (″). The calculated roughness (R) of sonochemically activated sample and the surface containing as-grown ZnO NSs is 56 and 149 nm.

The results indicated that forces and wave-driven streaming arising from the cavitation process create the proper roughness on the base substrate (R = 56 nm). In the case of ZnO deposited surface, the growth

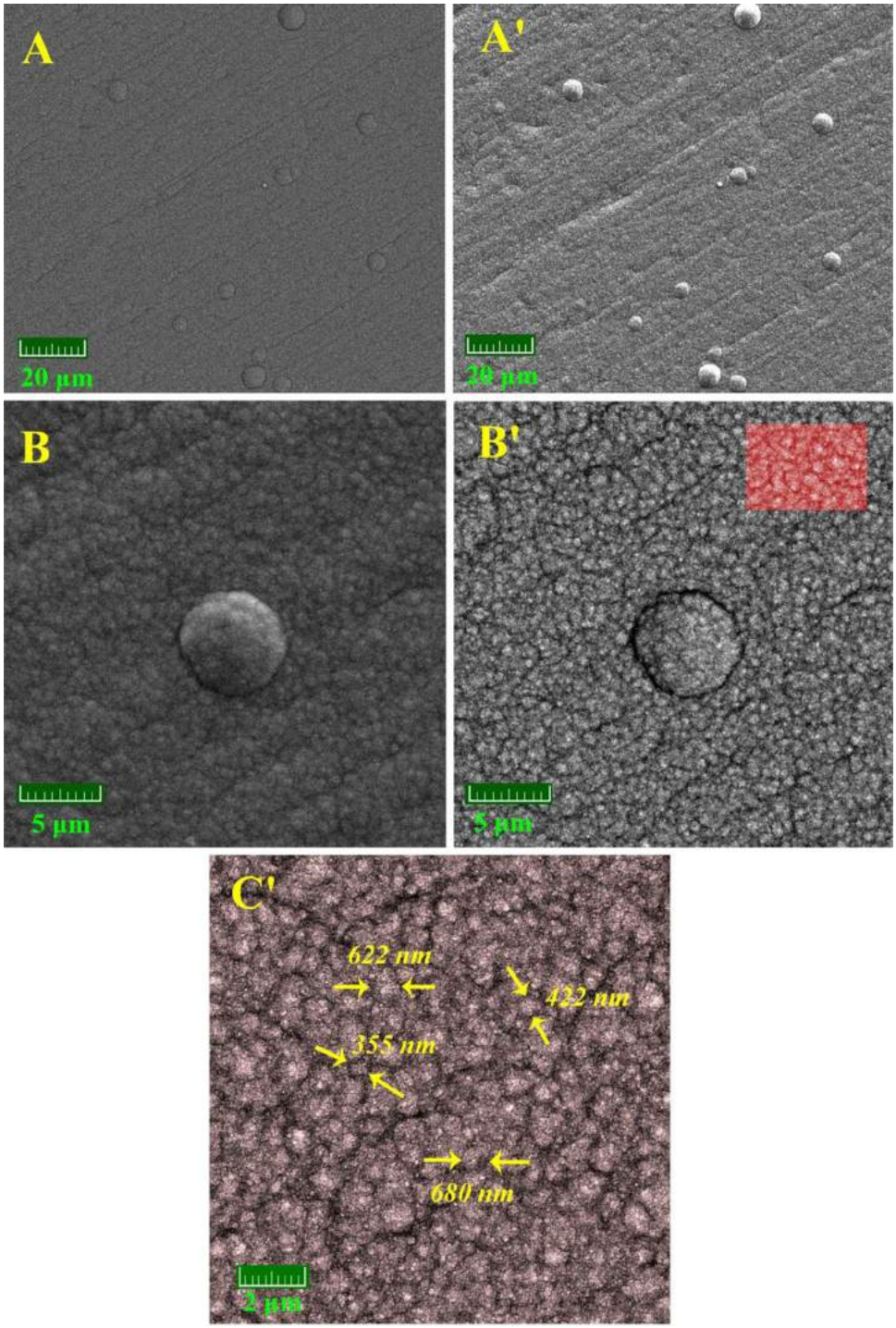

Fig. 4. The morphology of the *SZEN*: (A') and (B') are back backscatter images of (A) and (B), and (C') is a magnified view of the red shape marked on the image (B). (For interpretation of the references to colour in this figure legend, the reader is referred to the web version of this article).

of the zinc oxide nanostructures increases the roughness to 149 nm. As mentioned before, micro and nano-sized roughness formed during the activation process and especially after ZnO growth has a positive influence on increasing the density of active nucleation sites and contact surface area between the base substrate and the upper layer.

Fig. 7(A) and (B) refers to face projections of *SEN* and *SZEN*, respectively. (3D topographies and 3D phase images of each specimen are marked by the (′) and (″)).

The value of roughness for *SEN* and *SZEN* is 51.34 and 31.55 nm. The lower surface roughness of *SZEN* (compared to *SEN*) can be considered as the evidence for the increased uniformity of Ni-P coating. For a more detailed investigation, other phase images of *SEN* and *SZEN* are exhibited in Fig. 8.

This figure is provided for the comparison of Ni-P grain size in two above samples (the production of dense and fine-grained structures of Ni-P layer in *SZEN* could be clearly observed). Fig. 9 is a schematic view of the surface pretreatment, ZnO growth, the Ni electroless plating, and the formation of the Ni–P coating with fine grain on the surface with the underneath of ZnO NSs.

In the following section, the role of ZnO NSs in this observation is elaborated.

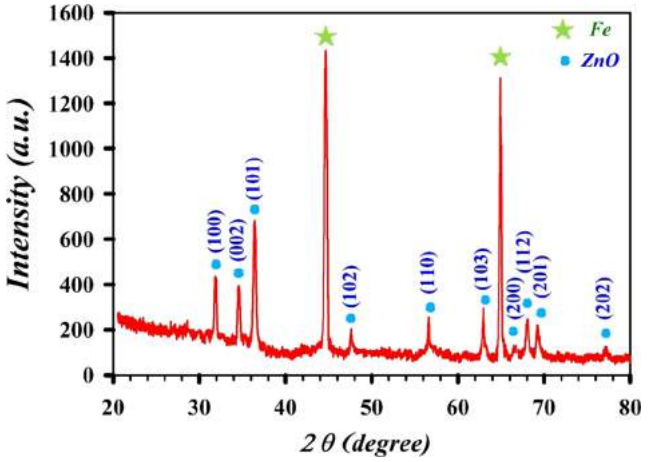

Fig. 5. The XRD results of the ZnO deposited sample.

3.2. Impact of ZnO synthesis on the deposition rate and the nucleation of Ni-P matrix

ZnO nanoflakes produce a high concentration of very fine and ultrafine sites for the nucleation and the crystal growth of Ni coating.

In EN plating, the metallic surface acts as substrate and catalyst too. The most probable mechanism (suggested in many literatures) includes the adsorption of Ni^{2+} cations on active sites of the metal surface and the chemical reduction of Ni^{2+} and P^{1+} to Ni and P by a reducing agent [32]:

$$Ni^{2+}_{ads} + H_2PO^-_{2ads} + H_2O \xrightarrow{cat} Ni^0 + 3H^+ + HPO^{2-}_3 \quad (1)$$

$$H_2PO^-_{2ads} + H_2O \xrightarrow{cat} HPO^{2-}_3 + H^+ + 2H_{ads} \quad (2)$$

$$H_2PO^-_{2ads} + H_{ads} \xrightarrow{cat} P^0 + H_2O + OH^- \quad (3)$$

$$2H_{ads} \xrightarrow{cat} H_2 \quad (4)$$

Since in electroless plating, the metallic substrate has a critical role in the initiation of the coating process, it seems that the growth of the ZnO nanostructures on the surface may reduce the Ni deposition rate. This predication affirmed by the study of the plating rate. Weighing samples before and after EN plating reveals that the deposition rate is reduced significantly in the presence of ZnO NSs. Moreover, the presence of this ceramic oxide causes a delay in initiating the plating process. However, after the diffusion of precursors to the underlying substrate, the nickel deposition begins, and the generation of a thin layer of Ni on the ZnO NSs as ultrafine nucleation sites occurs.

As mentioned, it has been reported that the ZnO is stable in alkaline media. However, the possibility of the partial dissolution of zinc oxide in the used bath was assumed. If this happens, the nano-sized roughness is generated due to dissolving nanosized ZnO structures. Furthermore, the co-deposition of Zn^{2+} cations may occur. The production of the nanosized roughness (as extra nucleation site), and also the incorporation of zinc into the Ni-P matrix and the formation of the ternary Zn-Ni-P have positive effects on properties of Ni coating. Not detection of zinc element in EDS analysis could be justified by the small

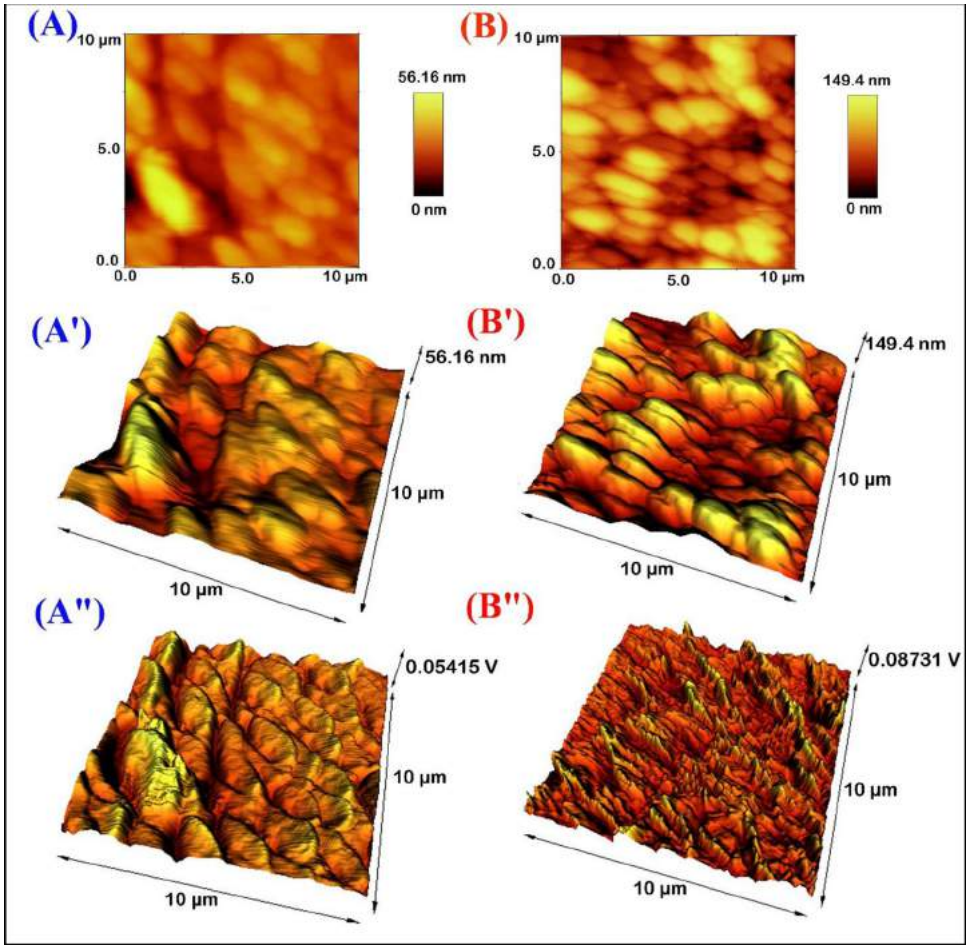

Fig. 6. The AFM results of the sono-treated sample and the ZnO-deposited surface: (A) and (B) refers to face projections. 3D topographies and 3D phase images of each specimen are marked by the (′) and (″).

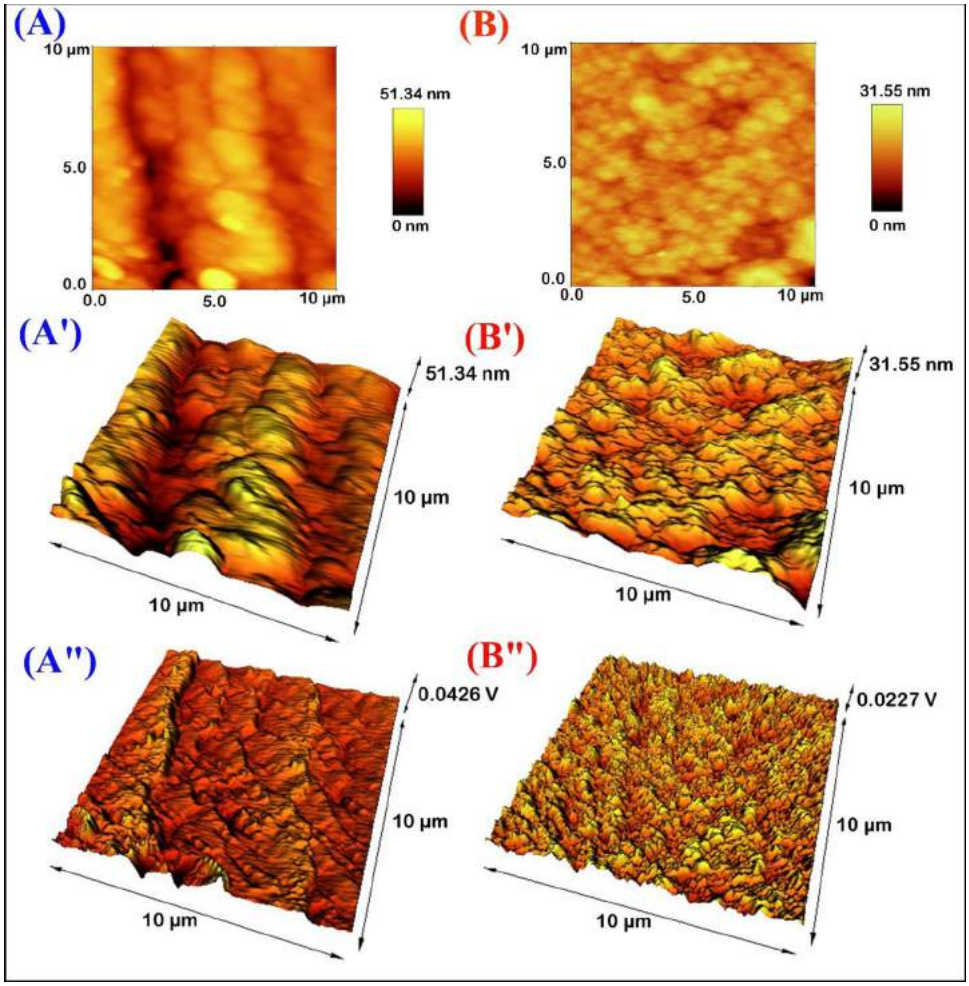

Fig. 7. The AFM results of EN plated samples: (A) and (B) refers to face projections of *SEN* and *SZEN*, respectively. (3D topographies and 3D phase images of each specimen are marked by the (′) and (″)).

amount of zinc deposition or covering a thin layer of Zn-Ni-P by a thick layer of Ni-P.

3.3. Corrosion study

PDP measurements were carried out and Tafel plots are shown in Fig. 10.

As seen in figure, the bare surface has the most negative circuit potential (E_{OCP} = -0.773 V) and the highest current density. The Ni-P plated sample (*SEN*) shows the positive shift in the open circuit potential (E_{OCP} = -0.432). Lower current density of this sample (compared to the bare substrate) indicates the reduced activity. In the case of *SZEN*, the most positive shift in E_{OCP} (E_{OCP} = -0.362 V) and the lowest current density confirm the lowest tendency to corrode.

The results of EIS measurements are presented as Nyquist plots in Fig. 11.

The equivalent circuit model used to fit the EIS experimental data is depicted in Fig. 11. The extracted parameters, including solution resistance (R_s), charge transfer resistance (R_{ct}), and constant phase element (CPE_{dl}), are summarized in Table 3. In addition, double layer capacitance values (C_{dl}) were obtained from CPE parameters according to the following equation [52]:

$$C_{dl} = P^{\frac{1}{n}} R_{ct}^{\frac{1-n}{n}} \quad (1)$$

where P and n are the magnitude of CPE and deviation parameter, respectively.

From the EIS analysis, the charge transfer resistance (R_{ct}) (considered as R_p) of *SEN* and *SZEN* is about 16,500 and 33,500 Ω cm^2, respectively. Furthermore, the lower value of double layer capacitance in EN plated samples (especially in *SZEN*) compared to the bare surface could be assigned to the existence of protective coatings. The coverage of the underlying surface and decreasing surface area, which acts as the site for charging, may be considered as the reason for the Cdl decrease in the sample with the underneath o zinc oxide nanostructures [52].

The reasons behind the enhanced corrosion resistance of the EN plated specimen with the underneath of ZnO nanostructures are described in the following section.

3.4. Corrosion and coating

The corrosion study of EN plated surfaces showed that the anticorrosive action of SEN is lower than SZEN. The existence of larger grains reduces the density and the uniformity of the nickel film in SEN. This property raises the possibility of the diffusion of corrosive species to the underlying surface and increases the corrosion rate. In the case of SZEN, ZnO nanostructures play a key role in the formation of the fine-grained nickel coating. This compact and uniform film could restrict the diffusion of corrosive species to the base substrate and improve the corrosion protection. The enhanced anticorrosive action of the Ni deposit can be influenced by physical and chemical properties of zinc oxide. ZnO is found as a semiconductor and thus covering the surface with ZnO structures leads to the restriction of electron transfer. This mechanism was suggested for the anticorrosive action of ZnO in organic coatings [29,30]. In the case of our study, zinc oxide by trapping

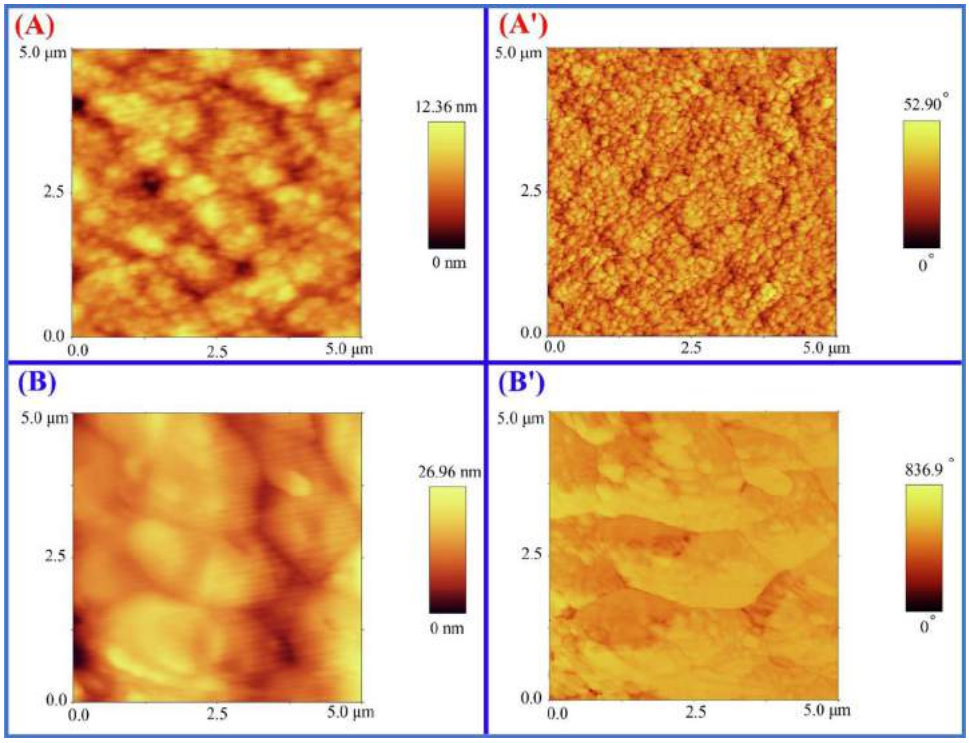

Fig. 8. Phase images of *SEN* ((A) and (A')), and *SZEN* ((B) and (B')).

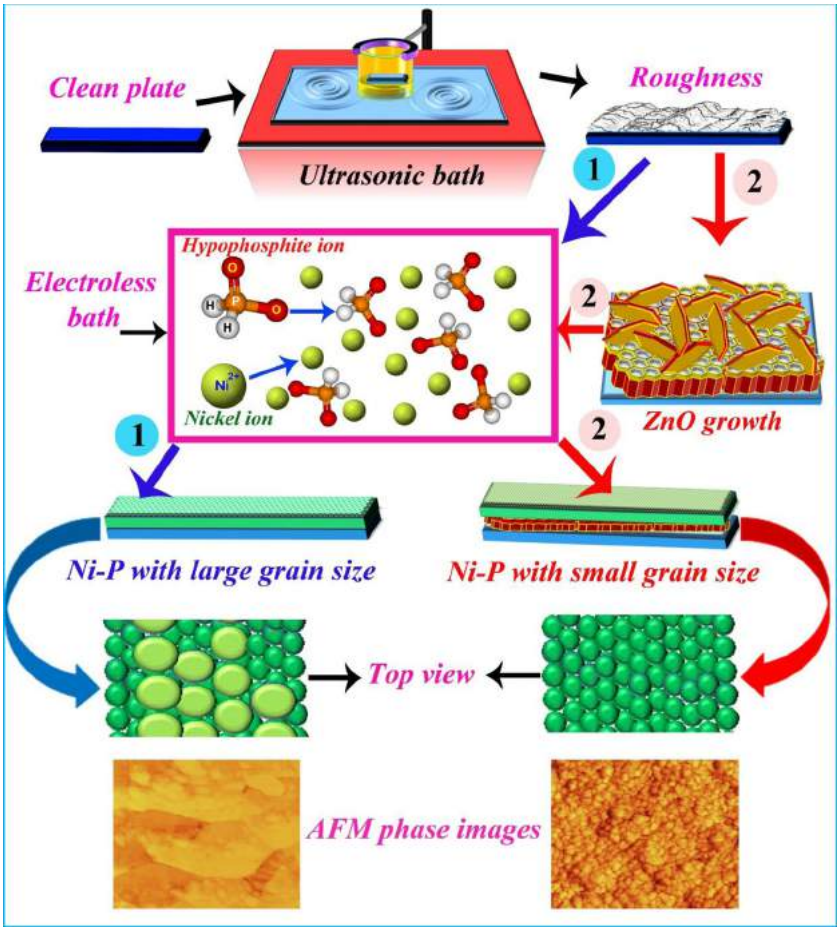

Fig. 9. A schematic view of the surface pretreatment, ZnO growth, the Ni electroless plating, and the formation of the Ni–P coating with fine grain size on the surface with the underneath of ZnO NSs.

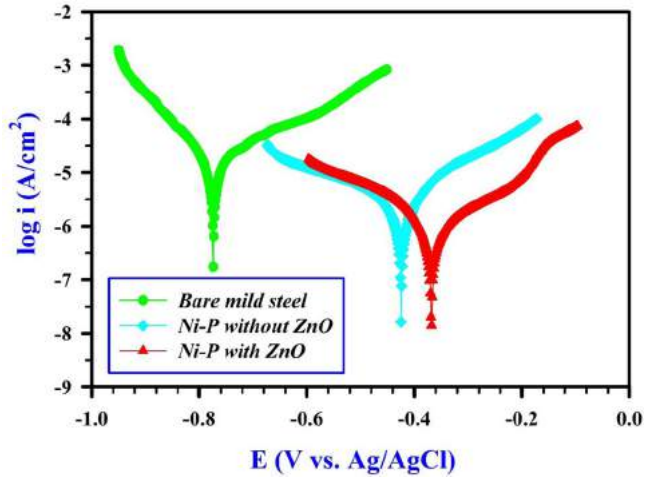

Fig. 10. Tafel plots of target samples.

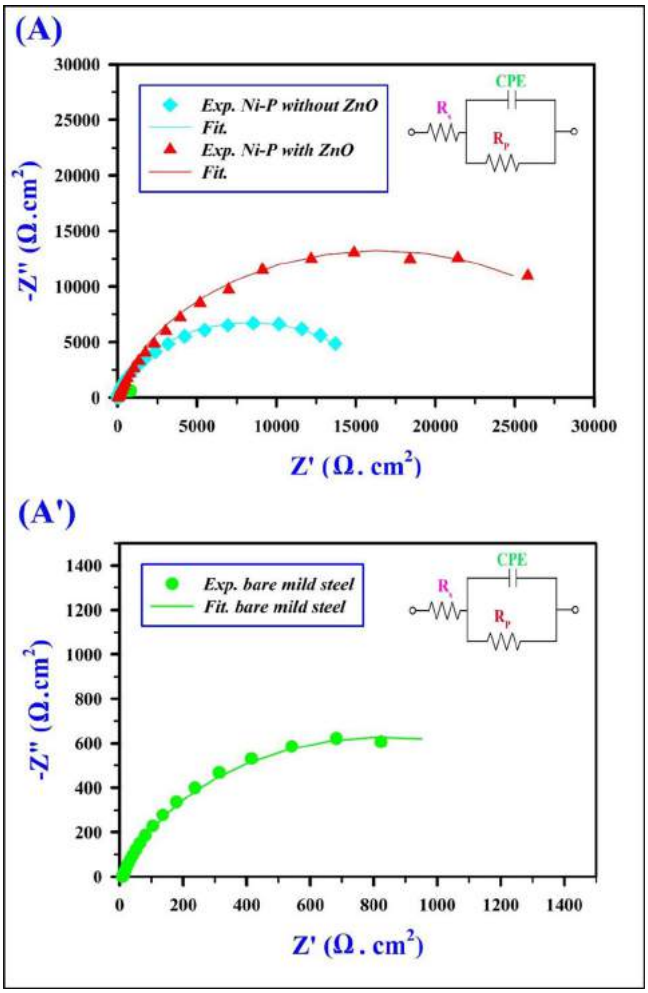

Fig. 11. Nyquist plots of samples.

electrons in the metal/solution interface can act as a barrier and reduces the metal dissolution. The physical effect of this matter may be attributed to the creation of the roughness on the bare surface. Based on open literature studies, structures with nanometric dimensions exhibit a higher electrical resistivity. This phenomenon is due to additional scattering centers, mainly from surface and grain boundaries [53]. Therefore, the considerable amount of ZnO nanoflakes (in SZEN) as scattering centers may result in an increased electrical resistivity.

Table 3
Electrochemical parameters extracted from EIS measurements.

Sample	R_s (Ω cm^2)	R_P (kΩ cm^2)	CPE_{dl}		Cdl (μF cm^{-2})
			P (μF cm^{-2} s^{n-1})	N	
Bare steel	8.87	1.65	1.611 × 10^3	0.82	19.88 × 10^2
SEN	6.87	16.60	29.11	0.87	26.12
SZEN	10.69	33.55	22.21	0.83	20.87

Additionally, ZnO nanosheets with different growth directions and the uniform distribution can operate as internal strength agents, and strengthen the Ni-P matrix.

Based on our experimental data, the growth of ZnO nanostructures on the surface has beneficial effects on the formation of a dense, uniform, and fine grained-size Ni-P layer with the improved anticorrosive performance. Regarding our results, the growth of zinc oxide as a safe and nontoxic agent through an easy and efficient way could be interested in the surface modification of the metallic surface before the EN plating as an engineering coating process.

4. Conclusion

In this paper, the surface modification of the mild steel surface by the deposition of zinc oxide as a safe, nontoxic, and chemical stable compound before electroless Ni plating was reported. The study of the morphology and surface roughness of EN plated surfaces with and without underneath of ZnO disclosed the role of this ceramic oxide in the formation of a dense, uniform, and fine-grained Ni-P layer. The role of ZnO nanostructures in the generation of active nucleation site density was investigated. In addition, the physical and chemical effects of ZnO on the corrosion behavior of Ni-P was discussed. Generating extra scattering centers, restricting electron transfer, and strengthening the Ni-P matrix were considered as reasons for the improved corrosion protection in the sample with ZnO NSs. Data reported in this literature could be useful to the access of the modified electroless Ni-P deposit as an important engineering coating.

Author statement

None.

Declaration of Competing Interest

None.

Acknowledgments

The support of Ferdowsi University of Mashhad (Mashhad, Iran) for this work is appreciated. We wish to express our gratitude to Mr. Khademi from Central Lab and Mrs. Majdi from Research and Technology of Ferdowsi University of Mashhad. We also acknowledge Mrs. Elham Hosseini from Central Research Laboratory of Mashhad University of Medical Sciences (Mashhad, Iran).

Appendix A. Supplementary data

Supplementary material related to this article can be found, in the online version, at doi:https://doi.org/10.1016/j.corsci.2020.108743.

References

[1] C. Buzea, I.I.P. Blandino, K. Robbie, Nanomaterials and nanoparticles: Sources and toxicity, Biointerphases 2 (2007) MR17–MR172.
[2] R. Jiang, D.T. Tran, J.P. McClure, D. Chu, Nano-structured bio-inorganic hybrid material for high performing oxygen reduction catalyst, ACS Appl. Mater. Interfaces

7 (2015) 18530–18539.
[3] R. Dastjerdi, M. Montazer, A review on the application of inorganic nano-structured materials in the modification of textiles: focus on anti-microbial properties, Colloids Surf. B 79 (2010) 5–18.
[4] W. He, H.K. Kim, W.G. Wamer, D. Melka, J.H. Callahan, J.J. Yin, Photogenerated charge carriers and reactive oxygen species in ZnO/Au hybrid nanostructures with enhanced photocatalytic and antibacterial Activity, J. Am. Chem. Soc. 136 (2014) 750–757.
[5] S.G. Kumar, K.S.R.K. Rao, Zinc oxide based photocatalysis: tailoring surface-bulk structure and related interfacial charge carrier dynamics for better environmental applications, RSC Adv. 5 (2015) 3306–3351.
[6] M. Laurenti, G. Canavese, S. Stassi, M. Fontana, M. Castellino, C.F. Pirri, V.A. Cauda, Porous nanobranched structure: an effective way to improve piezoelectricity in sputtered ZnO thin films, RSC Adv. 6 (2016) 76996.
[7] B. Kumar, S.W. Kim, Energy harvesting based on semiconducting piezoelectric ZnO nanostructure, Nano Energy 1 (2012) 342–355.
[8] I. Perelshtein, G. Applerot, N. Perkas, Wehrschetz-Sigl, A. Hasmann, G.M. Guebitz, A. Gedanken, Antibacterial properties of an in situ generated and simultaneously deposited nanocrystalline ZnO on Fabrics, ACS Appl. Mater. Interfaces 1 (2009) 361–366.
[9] N.C.T. Martins, C.S.R. Freire, C.P. Neto, A.J.D. Silvestre, J. Causio, G. Baldi, P. Sadocco, T. Trindade, Antibacterial paper based on composite coatings of nanofibrillated cellulose and ZnO, Colloids Surf. A 417 (2013) 111–119.
[10] P. Petkova, A. Francesko, I. Perelshtein, A. Gedanken, T. Tzanov, Simultaneous sonochemical-enzymatic coating of medical textiles with antibacterial ZnO nanoparticles, Ultrason. Sonochem. 29 (2016) 244–250.
[11] A. Yetisen, H. Qu, A. Manbachi, H. Butt, M.R. Dokmeci, J.P. Hinestroza, M. Skorobogatiy, A. Khademhosseini, S.H. Yun, Nanotechnology in textiles, ACS Nano 10 (2016) 3042–3068.
[12] K.H. Park, G.D. Han, K.C. Neoh, T.S. Kim, J.H. Shim, H.D. Park, Antibacterial activity of the thin ZnO film formed by atomic layer deposition under UV-A light, Chem. Eng. J. 328 (2017) 988–996.
[13] P. Petkova, A. Francesko, M.M. Fernandes, E. Mendoza, I. Perelshtein, A. Gedanken, T. Tzanov, Sonochemical coating of textiles with hybrid ZnO/chitosan antimicrobial nanoparticles, ACS Appl. Mater. Interfaces 6 (2014) 1164–1172.
[14] J. Deng, J. Ye, Y. Zhao, Y. Zhu, T. Wu, C. Zhang, L. Dong, H. Ouyang, X. Cheng, X. Wang, ZnO and hydroxyapatite-modified magnesium implant with a broad spectrum of antibacterial properties and a unique minimally invasive defined degrading capability, ACS Biomater. Sci. Eng. 5 (2019) 4285–4292.
[15] W. Wang, T.L. Li, H.M. Wong, P.K. Chu, R.Y.T. Kao, S. Wu, F.K.L. Leung, T.M. Wong, M.K.T. To, K.M.C. Cheung, K.W.K. Yeung, Development of novel implants with self-antibacterial performance through *in-situ* growth of 1D ZnO nanowire, Colloids Surf. B 141 (2016) 623–633.
[16] G. Ciofani, G.G. Genchi, V. Mattoli, ZnO nanowire arrays as substrates for cell proliferation and differentiation, Mater. Sci. Eng. C 32 (2012) 341–347.
[17] J.Y. Lee, B.S. Kang, B. Hicks, T.F. Chancellor, B.H. Chu, H.T. Wang, B.G. Keselowsky, F. Ren, T.P. Lele, The control of cell adhesion and viability by zinc oxide nanorods, Biomaterials 29 (2008) 3743–3749.
[18] J.K. Park, Y.J. Kim, J. Yeom, J.H. Jeon, G.C. Yi, J.H. Je, S.K. Hahn, The topographic effect of zinc oxide nanoflowers on osteoblast growth and osseointegration, Adv. Mater. 22 (2010) 4857–4861.
[19] S. Zhuang, M. Lu, N. Zhou, L. Zhou, D. Lin, Z. Peng, Q. Wu, Cu modified ZnO nanoflowers as photoanode material for highly efficient dye sensitized solar cells, Electrochim. Acta 294 (2019) 28–37.
[20] J. Tian, E. Uchaker, Q. Zhang, G. Cao, Hierarchically structured ZnO nanorods–nanosheets for improved quantum-dot-sensetized solar cells, ACS Appl. Mater. Interfaces 6 (2014) 4466–4472.
[21] V. Vaiano, G. Iervolino, L. Rizz, Cu-doped ZnO an efficient photocatalyst for the oxidation of arsenite to arsenate under visible light, Appl. Catal. B-Environ. 238 (2018) 471–479.
[22] Y.M. Hunge, M.A. Mahadik, A.V. Moholkar, C.H. Bhosale, Photoelectrocatalytic degradation of phthalic acid using spray deposited stratified WO_3/ZnO thin films under sunlight illumination, Appl. Surf. Sci. 420 (2017) 764–772.
[23] S.S.P. Selvin, A.G. Kumar, L. Sarala, R. Rajaram, A. Sathiyan, J.P. Merlin, I.S. Lydia, Photocatalytic degradation of rhodamine B using zinc oxide activated charcoal polyaniline nanocomposite and its survival assessment using aquatic animal model, ACS Sustain. Chem. Eng. 6 (2018) 258–267.
[24] J.E. Casillas, F. Tzompantzi, S.G. Castellanos, G. Mendoza-Damián, R. Pérez-Hernández, A. López-Gaona, A. Barrera, Promotion effect of ZnO on the photocatalytic activity of coupled Al_2O_3-Nd_2O_3-ZnO composites prepared by the sol − gel method in the degradation of phenol, Appl. Catal. B-Environ. 208 (2017) 161–170.
[25] F.H. Rajab, P. Korshed, Z. Liu, T. Wang, How did the structural ZnO nanowire as antibacterial coatings control the switchable wettability, Appl. Surf. Sci. 469 (2019) 593–606.
[26] T. Rezayi, M.H. Entezari, F. Moosavi, The variation of surface free energy of Al during superhydrophobicity processing, Colloid. Surface. A 322 (2017) 181–187.
[27] H. Liu, L. Feng, J. Zhai, L. Jiang, D. Zhu, Reversible wettability of a chemical vapor deposition prepared ZnO Film between superhydrophobicity and superhydrophilicity, Langmuir 20 (2004) 5659–5661.
[28] E. Velayi, R. Norouzbeigi, Annealing temperature dependent reversible wettability switching of micro/nano structured ZnO superhydrophobic surfaces, Appl. Surf. Sci. 441 (2018) 156–164.
[29] R. Najjar, S.A. Katourani, M.G. Hosseini, Self-healing and corrosion protection performance of organic polysulfide@urea-formaldehyde resin core-shell nanoparticles in epoxy/PANI/ZnO nanocomposite coatings on anodized aluminum alloy, Prog. Org. Coat. 124 (2018) 110–121.
[30] S.K. Dhoke, A.S. Khanna, T.J.M. Sinha, Effect of nano-ZnO particles on the corrosion behavior of alkyd-based waterborne coatings, Prog. Org. Coat. 64 (2009) 371–382.
[31] Z. Sharifalhoseini, M.H. Entezari, M. Shahidi, Synergistic effect of low and high intensity ultrasonic irradiation on the direct growth of ZnO nanostructures on the galvanized steel surface: investigation of the corrosion behavior, Ultrason. Sonochem. 44 (2018) 380–389.
[32] Z. Sharifalhoseini, M.H. Entezari, M. Shahidi, Direct growth of ZnO nanostructures on the Zn electroplated mild steel to create the surface roughness and improve the corrosion protection of the electroless Ni-P coating, Mater. Sci. Eng. B-Adv. 231 (2018) 18–27.
[33] D. Prasai, J.C. Tuberquia, R.R. Harl, G.K. Jennings, K.I. Bolotin, Graphene: corrosion-inhibiting coating, ACS Nano 6 (2012) 1102–1108.
[34] Y.P. Hsieh, M. Hofmann, K.W. Chang, J.G. Jhu, Y.Y. Li, K.Y. Chen, C.C. Yang, W.S. Chang, L.C. Chen, Complete corrosion inhibition through graphene defect passivation, ACS Nano 8 (2014) 443–448.
[35] Z.H. Xie, D. Li, Z. Skeete, A. Sharma, C.J. Zhong, Nanocontainer-enhanced self-healing for corrosion-resistant Ni coating on Mg Alloy, ACS Appl. Mater. Interfaces 9 (2017) 36247–36260.
[36] S.M. Popescu, A.J. Barlow, S. Ramadan, S. Ganti, B. Ghosh, J. Hedley, Electroless nickel deposition: an alternative for graphene contacting, ACS Appl. Mater. Interfaces 11 (2019) 16243–16251.
[37] H. Ashassi-Sorkhabi, M. Eshaghi, Corrosion resistance enhancement of electroless Ni–P coating by incorporation of ultrasonically dispersed diamond nanoparticles, Corros. Sci. 77 (2013) 185–193.
[38] W.W. Lee, J. Yi, S.B. Kim, Y.H. Kim, H.G. Park, W.I. Park, Morphology-controlled three-dimensional nanoarchitectures produced by exploiting vertical and in-plane crystallographic orientations in hydrothermal ZnO crystals, Cryst. Growth Des. 11 (2011) 4927–4932.
[39] H.M. Cheng, W.H. Chiu, C.H. Lee, S.Y. Tsai, W.F. Hsieh, Formation of branched ZnO nanowires from solvothermal method and dye-sensitized solar cells applications, J. Phys. Chem. C 112 (2008) 16359–16364.
[40] A.H.S. Rana, S.B. Chang, H.U. Chae, H. SeokKim, Structural, optical, electrical and morphological properties of different concentration sol-gel ZnO seeds and consanguineous ZnO nanostructured growth dependence on seeds, J. Alloys Compd. 729 (2017) 571–582.
[41] O. Lupan, T. Pauporté, B. Viana, I.M. Tiginyanu, V.V. Ursaki, R. Cortès, Epitaxial electrodeposition of ZnO nanowire arrays on p-GaN for efficient UV-light-emitting diode fabrication, ACS Appl. Mater. Interfaces 2 (2010) 2083–2090.
[42] K. Sakurai, M. Kanehiro, K. Nakahara, T. Tanabe, S. Fujita, S. Fujita, Effects of substrate offset angles on MBE growth of ZnO, J. Cryst. Growth 214-215 (2000) 92–94.
[43] A. Aravind, M.K. Jayaraj, M. Kumar, R. Chandra, The dependence of structural and optical properties of PLD grown ZnO films on ablation parameters, Appl. Surf. Sci. 286 (2013) 54–60.
[44] C.C. Wu, D.S. Wuu, P.R. Lin, T.N. Chen, R.H. Horng, Three-step growth of well-aligned ZnO nanotube arrays by self-catalyzed metalorganic chemical vapor deposition method, Cryst. Growth Des. 9 (2009) 4555–4561.
[45] X. Wen, Y. He, C. Chen, X. Liu, L. Wang, B. Yang, M. Leng, H. Song, K. Zeng, D. Li, K. Li, L. Gao, J. Tang, Magnetron sputtered ZnO buffer layer for Sb_2Se_3 thin film solar cells, Sol. Energy Mater. Sol. Cells 172 (2017) 74–78.
[46] H. Chen, W. Li, Q. Hou, H. Liu, L. Zhu, A general deposition method for ZnO porous films: occlusion electrosynthesis, Electrochim. Acta 56 (2011) 9459–9466.
[47] R.A. Picca, M.C. Sportelli, D. Hötger, K. Manoli, C. Kranz, B. Mizaikoff, L. Torsi, N. Cioffi, Electrosynthesis and characterization of ZnO nanoparticles as inorganic component in organic thin-film transistor active layers, Electrochim. Acta 178 (2015) 45–54.
[48] J.S. Huang, C.Y. Lee, T.S. Chin, Forming-free bipolar memristive switching of ZnO films deposited by cyclic-voltammetry, Electrochim. Acta 91 (2013) 62–68.
[49] A. Aranda, R. Landers, P. Carnelli, R. Candal, H. Alarcón, J. Rodríguez, Influence of silver electrochemically deposited onto zinc oxide seed nanoparticles on the photoelectrochemical performance of zinc oxide nanorod films, Nanomater. Nanotechnol. 9 (2019) 1–9.
[50] Z. Sharifalhoseini, M.H. Entezari, The new aspects of the anticorrosive ZnO@SiO_2 core–shell NPs in stabilizing of the electrolytic Ni bath and the Ni coating structure; electrochemical behavior of the resulting nano-composite coatings, J. Colloid Interface Sci. 455 (2015) 110–116.
[51] Z. Sharifalhoseini, M.H. Entezari, Mohsen Shahidi, Mechanistic investigation of the influence of phosphoric and boric acids in the formation of homogeneous Ni–P/ZnO@SiO_2 coatings, J. Colloid Interface Sci. 464 (2016) 291–300.
[52] A. Kosari, M.H. Moayed, A. Davoodi, R. Parvizi, M. Momeni, H. Eshghi, H. Moradi, Electrochemical and quantum chemical assessment of two organic compounds from pyridine derivatives as corrosion inhibitors for mild steel in HCl solution under stagnant condition and hydrodynamic flow, Corros. Sci. 78 (2014) 138–150.
[53] H. Marom, M. Eizenberg, The effect of surface roughness on the resistivity increase in nanometric dimensions, J. Appl. Phys. 99 (2006) 123705.